Higher Harmonic Analyses of the Rossi-α Method and Application of Dynamic Mode Decomposition for Time Decay Constant Determination in a 1D Subcritical System

Toshihiro Yamamoto[a*], Hiroki Sakamoto[b]

[a]*Institute for Integrated Radiation and Nuclear Science, Kyoto University, 2 Asashiro Nishi, Kumatori-cho, Sennan-gun, Osaka, 590–0494, Japan*
[b]*Independent researcher, Radiation Dose Analysis and Evaluation Network, 4–13–14, Kokubunji-shi, Tokyo, 185–0001, Japan*

Abstract

An exact formula for the joint probability of pair neutron detection for the Rossi-α method, which is composed of the sum of a large number of higher harmonics, is verified in this study by comparing it with a Monte Carlo simulation. A simple conventional formula for the Rossi-α method cannot yield an accurate fundamental mode time-decay constant α owing to the effect of higher harmonics. Dynamic mode decomposition (DMD) is applied to the eigendecomposition of autocorrelation functions in a subcritical system. Through DMD, the autocorrelations obtained from the deterministic exact formula, which is free from stochastic noise, are accurately decomposed into major higher harmonic components. The DMD results obtained from a Monte Carlo simulation are inferior to the deterministic results due to stochastic noise. These findings suggest that if detection positions are properly allocated within a subcritical system, DMD can yield a satisfactorily accurate fundamental mode α-eigenvalue.

Keywords: Rossi- α ; subcriticality measurement; higher harmonics; dynamic mode decomposition; Monte Carlo

1. Introduction

Among many subcriticality measurement techniques, the Rossi-α method (Orndoff, 1957) is a well-known and widely used noise technique along with the Feynman-α method (Feynman et

* Corresponding author
E-mail address: yamamoto.toshihiro.8u@kyoto-u.ac.jp (T. Yamamoto)

al., 1956). The Rossi-α method measures the prompt neutron time-decay constant α using the neutron detection correlation between two different detection times. If space- and energy-dependence is ignored, the correlation simply decays with a single time-decay constant, i.e., the fundamental mode α. However, in reality, the difficulty in determining α, which arises with space- and energy-dependence, is that the correlation decays with multiple time-decay constants (Iijima et al., 1968). Applying a well-known simple formula for the Rossi-α method, $Ae^{-\alpha t} + B$, would yield an α-value that significantly deviates from the fundamental mode α-eigenvalue. Furthermore, the deviation is space-dependent and depends on the time interval used for the regression analysis. Some attempts were made to extract the fundamental mode α from the correlation that decays with multiple time-decay constants (Berglöf et al., 2011; Szieberth et al., 2015; Talamo et al., 2020). Talamo et al. (2013) developed a method by introducing a correction factor to reproduce a fundamental mode α-eigenvalue. For the pulsed neutron method, a similar study was performed by Katano (2019) using the "linear combination method".

The first part of this study addresses the higher harmonic analysis in the Rossi-α method. Muñoz-Cobo et al. (2011) and Yamamoto (2011a, 2014, 2015) performed higher harmonic analyses for the Feynman-α method and the ^{252}Cf source-driven noise analysis method based on the exact space- and energy-dependent noise theory by Endo et al. (2006). The exact formula was verified through the precise agreement between the theoretical values and the Monte Carlo simulations of the measurement techniques. Using the same procedure as in these previous works, higher harmonic analyses of the Rossi-α method are performed in the first part of this study.

An alternative approach to extract the fundamental mode time-decay constant in addition to the previously developed techniques mentioned above (e.g., Berglöf et al., 2011; Szieberth et al., 2015) is to introduce a data-driven technique that is available for analyzing dynamical time-varying systems. Dynamic mode decomposition (DMD) is a data-driven technique (Schmid, 2010; Kutz et al., 2016). DMD first appeared in the fluid dynamics field and has become increasingly popular in the nuclear engineering field. The applications of DMD in nuclear engineering include isotopic evolution analysis (Abdo et al., 2019), acceleration of discrete ordinates radiative transfer

calculations (McClarren and Haut, 2020), stability analysis of the molten salt reactor (Di Ronco et al., 2020), acceleration of the power iteration method for *k*-eigenvalue calculations (Roberts, et al., 2019), and analysis of the time-decay constant α in a pulsed neutron experiment (McClarren, 2019; Hardy et al., 2019). The authors recently applied DMD to determine the spatial decay constant in an exponential experiment (Yamamoto and Sakamoto, 2021). In the second part of this study, DMD was newly applied to the neutron noise technique for subcriticality measurement with the Rossi-α method. The applicability of DMD to the determination of the time-decay constant α in the Rossi-α method is examined in the following sections.

2. Higher harmonics analysis of Rossi-α

In this section, following the previous literature (Endo et al., 2006; Yamamoto 2011a; Yamamoto, 2014; Yamamoto, 2015), a formula for decomposing the joint probability of a pair neutron detection in two different times into the sum of the higher harmonics is revisited. Although the formulation should be presented in transport theory, a higher harmonic analysis that considers a large number of higher harmonics is challenging in transport theory. In (Kophazi et al., 2012) and (Szieberth et al., 2017), the higher harmonics of the VENUS-F subcritical assembly were calculated up to the first ten modes in a transport code. On the other hand, Uyttenhove et al. (2014) shows that the diffusion approximation is more feasible since more than 100 modes were calculated for the same problem with a diffusion code. Thus, the formulation is presented based on the multigroup diffusion theory. As demonstrated in Section 4, diffusion theory can yield satisfactorily accurate results for a simple problem treated in this study. Delayed neutrons were not considered throughout this study.

Suppose that neutrons are emitted in a subcritical system from an external neutron source that distributes according to a spatial distribution $S(\boldsymbol{r})$ and has an energy spectrum χ_s^g. The joint probability of a pair neutron detection within the infinitesimal duration dt_1 around t_1 and dt_2 around t_1 $(t_2 > t_1)$ is given as a function of the time lag $\tau\ (= t_2 - t_1)$ (Endo et al., 2006):

$$P(\tau, \boldsymbol{r})dt_1 dt_2 = \sum_{n=0}^{\infty} A_n(\tau, \boldsymbol{r})dt_1 dt_2 + C_R(\boldsymbol{r})^2 dt_1 dt_2, \tag{1}$$

where

$$A_n(\tau, \boldsymbol{r}) = e^{-\alpha_n \tau} \sum_{m=0}^{\infty} \sum_{k=0}^{\infty} \frac{S_k F_{kmn} C_m(\boldsymbol{r}) C_n(\boldsymbol{r})}{\alpha_k(\alpha_m + \alpha_n)}. \quad (2)$$

It is assumed that only one neutron is emitted at one source emission. A high frequency D-D or D-T external neutron source or Am-Be neutron source satisfies this assumption. On the other hand, a ^{252}Cf external neutron source is not available. Thus, the correlation between multiple neutrons from the source emission needs not be considered. Furthermore, a detected neutron is absorbed immediately and does not contribute to the subsequent reactions. While a ^{3}He or ^{10}B detector is available for this assumption, a fission chamber detector is not. The terms included in Eq. (2) are defined as follows:

$$S_k = \int_V d\boldsymbol{r} S(\boldsymbol{r}) \Psi^*_{s,k}(\boldsymbol{r}), \quad (3)$$

where

$$\Psi^*_{s,k}(\boldsymbol{r}) = \sum_{g=1}^{G} \chi_s^g \psi^*_{g,k}(\boldsymbol{r}). \quad (4)$$

$\int_V d\boldsymbol{r}$ denotes the volume integral over the entire region. $\psi^*_{g,k}(\boldsymbol{r})$ in Eq. (4) is the adjoint flux of the energy Group g and kth harmonic and is defined as an eigenfunction of Eq. (10) shown below. The first term on the right-hand side of Eq. (1) represents a correlation between the progenies arising from a fission event, and the second term is the uncorrelated term arising from the different ancestors. $C_R(\boldsymbol{r})$ is the steady-state neutron count rate and is defined as follows:

$$C_R(\boldsymbol{r}) = \sum_{k=0}^{\infty} \frac{S_k C_k(\boldsymbol{r})}{\alpha_k}, \quad (5)$$

where α_k is the α-eigenvalue of kth harmonic, and

$$C_k(\boldsymbol{r}) = \sum_{g=1}^{G} \int_V \Sigma_{d,g} \delta(\boldsymbol{r}' - \boldsymbol{r}) \psi_{g,k}(\boldsymbol{r}') d\boldsymbol{r}', \quad (6)$$

where $\Sigma_{d,g}$ is the detection cross section of the energy Group g and $\psi_{g,k}(\boldsymbol{r})$ is the forward flux of the Group g and kth harmonic. F_{kmn} in Eq. (2) is defined as follows:

$$F_{kmn} = \sum_{g=1}^{G} \int_V \overline{\nu(\nu-1)} \Sigma_{f,g}(\boldsymbol{r}) \psi_{g,k}(\boldsymbol{r}) \Psi^*_{f,m}(\boldsymbol{r}) \Psi^*_{f,n}(\boldsymbol{r}) d\boldsymbol{r}, \quad (7)$$

where $\overline{\nu(\nu-1)}$ is the Diven factor, $\Sigma_{f,g}$ is the fission cross section in Group g, and

$$\Psi^*_{f,m}(\boldsymbol{r}) = \sum_{g=1}^{G} \chi_f^g \psi^*_{g,m}(\boldsymbol{r}), \tag{8}$$

where χ_f^g is the energy spectrum of fission neutrons. The forward and adjoint fluxes in the α-eigenvalue mode are, respectively, the eigenfunctions of the diffusion equations as follows:

$$\boldsymbol{M_g}(\boldsymbol{r})\psi_{g,m}(\boldsymbol{r}) = \frac{\alpha_m}{v_g}\psi_{g,m}(\boldsymbol{r}), \tag{9}$$

$$\boldsymbol{M^*_g}(\boldsymbol{r})\psi^*_{g,m}(\boldsymbol{r}) = \frac{\alpha_m}{v_g}\psi^*_{g,m}(\boldsymbol{r}), \tag{10}$$

where v_g is the neutron velocity of Group g. The differential operators, $\boldsymbol{M_g}(\boldsymbol{r})$ and $\boldsymbol{M^*_g}(\boldsymbol{r})$, are defined as follows:

$$\begin{aligned}\boldsymbol{M_g}(\boldsymbol{r})\psi_{g,m}(\boldsymbol{r}) &\equiv -\nabla D_g(\boldsymbol{r})\cdot\nabla\psi_{g,m}(\boldsymbol{r}) + \Sigma_{a,g}(\boldsymbol{r})\psi_{g,m}(\boldsymbol{r}) + \sum_{\substack{g'=1\\ g\neq g'}}^{G}\Sigma_s^{g\to g'}(\boldsymbol{r})\psi_{g,m}(\boldsymbol{r}) \\ &\quad - \chi_f^g\sum_{g'=1}^{G}\nu\Sigma_{f,g'}(\boldsymbol{r})\psi_{g',m}(\boldsymbol{r}) - \sum_{\substack{g'=1\\ g\neq g'}}^{G}\Sigma_s^{g'\to g}(\boldsymbol{r})\psi_{g',m}(\boldsymbol{r}).\end{aligned} \tag{11}$$

$$\begin{aligned}\boldsymbol{M^*_g}(\boldsymbol{r})\psi^*_{g,m}(\boldsymbol{r}) &\equiv -\nabla D_g(\boldsymbol{r})\cdot\nabla\psi^*_{g,m}(\boldsymbol{r}) + \Sigma_{a,g}(\boldsymbol{r})\psi^*_{g,m}(\boldsymbol{r}) + \sum_{\substack{g'=1\\ g\neq g'}}^{G}\Sigma_s^{g\to g'}(\boldsymbol{r})\psi^*_{g,m}(\boldsymbol{r}) \\ &\quad - \nu\Sigma_{f,g}(\boldsymbol{r})\sum_{g'=1}^{G}\chi_f^{g'}\psi^*_{g',m}(\boldsymbol{r}) - \sum_{\substack{g'=1\\ g\neq g'}}^{G}\Sigma_s^{g\to g'}(\boldsymbol{r})\psi^*_{g',m}(\boldsymbol{r}).\end{aligned} \tag{12}$$

where D_g is the diffusion coefficient, $\Sigma_{a,g}$ is the absorption cross section, and $\Sigma_s^{g\to g'}$ is the scattering cross section from group g to g'. The forward and adjoint eigenfunctions have the

following orthonormal relationship:

$$\sum_{g=1}^{G}\int_{V}\frac{1}{v_g}\psi_{g,m}^{*}(\boldsymbol{r})\psi_{g,n}(\boldsymbol{r})d\boldsymbol{r}=\delta_{m,n}, \tag{13}$$

where $\delta_{m,n}$ is the Kronecker delta.

3. DMD of the Rossi-α method

In a subcritical measurement with the Rossi-α method, time series data of neutron detections are obtained for a steady-state subcritical state. Many types of signal processing methods (e.g., Type-I Rossi-α, Type-II Rossi-α (Kitamura et al., (1999)), and autocorrelation function method (Szieberth et al. (2015)) have been proposed for the Rossi-α method. This study adopted a method where the autocorrelation function is used as the joint probability of pair neutron detection. In this study, the time series data are composed of a large number of time bins, each of which stores the number of neutron counts. Using the time series data, the autocorrelations are given by

$$x_{i,k}=\frac{1}{M-k}\sum_{m=1}^{M-k}c_{i,m}c_{i,m+k}\,,\quad k=1,\dots,J<M-1, \tag{14}$$

where M is the number of time bins, i is the position index of the detector, $c_{i,m}$ is the number of neutron counts in the mth time bin, and k is the time lag index. The time lag for the lag index k is $k\Delta$, where Δ is the time interval of each time bin. The autocorrelation, $x_{i,k}$, decreases with the time lag index k because of the decay of the correlated term until it asymptotically reaches the square of mean counts in each time bin. In Eq. (14), $x_{i,k}$ is calculated up to the time lag index J. This maximum time lag index J is determined such that $x_{i,k}$ sufficiently decreases and reaches equilibrium before $k=J$.

The details of DMD are already presented extensively in many publications. An overview of DMD that focuses on application to the Rossi-α method is described in this section. The DMD algorithm in this section is based on the description in Chapter 1 in (Kutz et al., 2016), which is the same as the one used for an exponential experiment in (Yamamoto and Sakamoto, 2021).

Suppose that time series data for the Rossi-α method are measured at n positions in a subcritical system. The set of n autocorrelations for the kth lag index constitutes an n-dimensional

column vector:

$$\mathbf{x}_k = \left[x_{1,k}\ x_{2,k} \ldots\ x_{i,k} \ldots x_{n,k}\ \right]^T, \tag{15}$$

where $x_{i,k}$ is the autocorrelation of the ith position for the time lag $k\Delta$. Each $\mathbf{x}_k$ is regarded as a snapshot in the dynamic mode. The DMD algorithm in this study constitutes the vector $\mathbf{x}_k$ at equally spaced time lag Δ for $k = 1, \ldots, J$, where J is a time lag before which $\mathbf{x}_k$ already reaches an equilibrium state. Using $\mathbf{x}_k$ for $k = 1, \ldots, J$, the two matrices required by the DMD algorithm are defined as follows:

$$\mathbf{X} = \left[\mathbf{x}_1\ \mathbf{x}_2 \ldots\ \mathbf{x}_j \ldots \mathbf{x}_{J-1}\right], \tag{16}$$

$$\mathbf{X}' = \left[\mathbf{x}_2\ \mathbf{x}_3 \ldots\ \mathbf{x}_j \ldots \mathbf{x}_J\right]. \tag{17}$$

The dimensions of $\mathbf{X}$ and $\mathbf{X}'$ are both $n \times (J-1)$. A linear operator matrix $\mathbf{A}$ is assumed to exist such that $\mathbf{X}$ is linearly connected to $\mathbf{X}'$ as follows:

$$\mathbf{X}' \approx \mathbf{A}\mathbf{X}. \tag{18}$$

The best-fit linear operator matrix $\mathbf{A}$ with dimensions of $n \times n$ is given as follows:

$$\mathbf{A} = \mathbf{X}'\mathbf{X}^{\dagger}, \tag{19}$$

where $\dagger$ denotes the Moore−Penrose pseudo−inverse. A singular value decomposition is performed for $\mathbf{X}$ as follows:

$$\mathbf{X} = \mathbf{U}\mathbf{\Sigma}\mathbf{V}^{*}, \tag{20}$$

where the asterisk $*$ indicates the conjugate transpose. The dimensions of $\mathbf{U}, \mathbf{\Sigma}, \text{and } \mathbf{V}$ are $n \times n$, $n \times n$, and $(J-1) \times n$, respectively. A low-rank truncation to $\mathbf{U}$, $\mathbf{\Sigma}$, and $\mathbf{V}$ might yield optimal solutions that minimize $\|\mathbf{X}' - \mathbf{A}\mathbf{X}\|_2$. After a low-rank $r(\leq \min(n, J-1))$ is chosen, $\mathbf{X}$ is approximated by the truncated matrices:

$$\mathbf{X} \approx \mathbf{U}_{\mathrm{r}}\mathbf{\Sigma}_{\mathrm{r}}\mathbf{V}_{\mathrm{r}}^{*}, \tag{21}$$

where $\mathbf{U}_{\mathrm{r}} \in \mathbb{C}^{\mathrm{n}\times\mathrm{r}}, \mathbf{\Sigma}_{\mathrm{r}} \in \mathbb{C}^{\mathrm{r}\times\mathrm{r}}$, and $\mathbf{V}_{\mathrm{r}} \in \mathbb{C}^{(\mathrm{J}-1)\times\mathrm{r}}$. Using $\mathbf{U}_{\mathrm{r}}$, $\mathbf{\Sigma}_{\mathrm{r}}$, and $\mathbf{V}_{\mathrm{r}}$, the pseudo−inverse of $\mathbf{X}$ is given as follows:

$$\mathbf{X}^{\dagger} = \mathbf{V}_{\mathrm{r}}\mathbf{\Sigma}_{\mathrm{r}}^{-1}\mathbf{U}_{\mathrm{r}}^{*}. \tag{22}$$

The rank reduction of the matrix $\mathbf{A}$ from $n \times n$ to $r \times r$ is given as follows:

$$\widetilde{\mathbf{A}} = \mathbf{U}_{\mathrm{r}}^{*}\mathbf{A}\mathbf{U}_{\mathrm{r}} = \mathbf{U}_{\mathrm{r}}^{*}\mathbf{X}'\mathbf{V}_{\mathrm{r}}\mathbf{\Sigma}^{-1}. \tag{23}$$

The mapping from $\mathbf{A}$ to $\widetilde{\mathbf{A}}$ is a similarity transformation, and both matrices have the same eigenvalues. Performing the eigendecomposition of $\widetilde{\mathbf{A}}$, we have

$$\widetilde{\mathbf{A}}\mathbf{W} = \mathbf{W}\mathbf{\Lambda}, \tag{24}$$

where columns of $\mathbf{W}$ are eigenvectors and $\mathbf{\Lambda}$ is a diagonal matrix containing the corresponding eigenvalues λ_m $(1 \leq m \leq r)$. The eigenvalues of $\mathbf{A}$ are the diagonal components of $\mathbf{\Lambda}$, and the eigenvectors of $\mathbf{A}$ are given by the columns of $\mathbf{\Phi}$:

$$\mathbf{\Phi} = \mathbf{X}'\mathbf{V}_r\mathbf{\Sigma}_r^{-1}\mathbf{W}. \tag{25}$$

The transition of the vector $\mathbf{x}$ with respect to the time lag τ is approximated by introducing a linear mapping operator $\mathbf{B}$:

$$\frac{d\mathbf{x}(\tau)}{d\tau} = \mathbf{B}\mathbf{x}. \tag{26}$$

The solution to this differential equation is given as follows:

$$\mathbf{x}(\tau) = \mathbf{x}(\mathbf{0})\boldsymbol{e}^{\mathbf{B}\tau}. \tag{27}$$

Since $\mathbf{X}'$ represents a time advancement of Δ compared to $\mathbf{X}$, and according to Eq. (18) is connected to it by a local linear approximation, the matrix $\mathbf{A}$ is equivalent to the discrete-time approximation to $\boldsymbol{e}^{\mathbf{B}\Delta}$. The continuous-time eigenvalue, i.e., the α-eigenvalue, corresponds to the discrete eigenvalue λ_m of $\mathbf{A}$ as follows:

$$\lambda_m = \exp(\alpha_m \Delta). \tag{28}$$

Using the eigenvalues and eigenvectors of $\mathbf{A}$, the snapshots of the autocorrelation as a function of the time lag τ are approximately reproduced by:

$$\mathbf{x}(\tau) \approx \mathbf{\Phi} \exp(\mathbf{\Gamma}\tau)\, \mathbf{b}, \tag{29}$$

where

$$\mathbf{b} = [b_1\ b_2\ \ldots\ b_m\ \ldots\ b_r\ ]^T, \tag{30}$$

b_m is the amplitude of the mth mode for the minimum time lag $k = 1$, and $\mathbf{\Gamma}$ is an $r \times r$ diagonal matrix with the mth entry equal to

$$\alpha_m = \frac{\ln(\lambda_m)}{\Delta}. \tag{31}$$

Because $\mathbf{x}_1 = \mathbf{x}(0) = \mathbf{\Phi}\mathbf{b}$, the amplitude vector at the minimum time lag is given as follows:

$$\mathbf{b} = \mathbf{\Phi}^{\dagger}\mathbf{x}_1, \tag{32}$$

where $\mathbf{\Phi}^{\dagger}$ is the Moore−Penrose pseudo−inverse of $\mathbf{\Phi}$.

4. Rossi-α method simulation

4.1 Problem description

The DMD method described in Section 3 was applied to a numerical model simulating the Rossi-α method in a one-dimensional multigroup subcritical system. The model was composed of three infinitely long slabs where two homogenized light-water moderated UO_2 fuel rod regions were separated by a light water slab with a thickness of 16 cm, as shown in Fig. 1. The neutron interaction between the two fuel regions was relatively weak. This subcritical system can be classified as a "decoupled system". The close separation of α-eigenvalues between the fundamental mode and first harmonic is anticipated. Thus, this test problem is challenging because it may have difficulty discriminating between the fundamental mode and first harmonic from the autocorrelation function. The numerical simulations were performed with two-energy group constants that are listed in Table 1. A neutron source that solely emitted a fast neutron with a Poisson process timing was placed 25.4 cm from the left boundary. The source was intentionally located off-center to activate the asymmetric harmonics. The source intensity was 8000 neutrons/s. Neutrons were detected at 44 points, as indicated in Fig. 1. The detector cross section $\Sigma_{d,g}$ in Eq. (6) was the capture cross section in each region in the thermal energy group.

Table 1 Group constants

	Fuel zone	Water
D_1 (cm)	1.45294	0.905414
D_2(cm)	0.197177	0.125647
Σ_{t1} (cm^{-1})	0.229420	0.368156
Σ_{t2}(cm^{-1})	1.69053	2.65294
Σ_{f1} (cm^{-1})*	0.00268003	0
Σ_{f2}(cm^{-1})*	0.0646204	0
ν	2.4	0
$\overline{\nu(\nu-1)}$	3.6	0
Σ_{a1} (cm^{-1})	0.009641573	0.000460058
Σ_{a2}(cm^{-1})	0.1174147	0.0188813
$\Sigma_s^{1\to2}$ (cm^{-1})	0.0225209	0.0584208
v_1(cm/s)	2.8×10^7	2.8×10^7
v_2(cm/s)	3.0×10^5	3.0×10^5

*For the diffusion calculations, the fission cross sections were multiplied by 0.994963 for adjusting the criticality.

4.2 Results of eigenvalue and fixed source calculations.

The fixed source and α-eigenvalue mode calculations were performed with both the diffusion-based deterministic method and Monte Carlo method. Isotropic scattering was assumed for the Monte Carlo calculations. The diffusion coefficients were given by $1/(3\Sigma_t)$. The higher harmonic analyses in this study used the diffusion code RHEINGOLD (Yamamoto, et al., 2003; Yamamoto and Sakamoto, 2019; Yamamoto and Sakamoto, 2021) for eigendecomposition of the one-dimensional flux distribution in the steady state subcritical system. For the diffusion calculations, a standard extrapolated boundary condition was imposed on the left and right boundaries (i.e., $-D\nabla\phi/\phi = 0.4692$). The entire geometry was discretized into a 301 mesh (120 for each fuel region and 61 for the water region).

The one-dimensional steady-state neutron flux distribution, $\phi_g^s(x)$, can be expanded using the eigenfunctions of Eq. (9) as follows:

$$\phi_g^s(x) = \sum_{m=0}^{\infty} a_m \psi_{g,m}(x), \tag{33}$$

where a_m is the expansion coefficient of the *m*th eigenfunction. Using orthogonality relations of Eq. (13), the expansion coefficient is given as follows:

$$a_m = \frac{\langle \psi_{g,m}^*(x) \frac{1}{v_g} \phi_g^s(x) \rangle}{\langle \psi_{g,m}^*(x) \frac{1}{v_g} \psi_{g,m}^*(x) \rangle}. \tag{34}$$

The relative expansion coefficients a_m (up to 5th higher harmonic) with respect to the fundamental mode are shown in Table 2. Fig. 2 shows the spatial distribution of the fundamental mode and higher harmonics up to the 4th order that were decomposed from the steady-state thermal neutron flux distribution, $\phi_2^s(x)$. The reconstructed flux distribution that was obtained by summing all higher harmonic components (up to 602 modes) is also shown in Fig. 2 The reconstructed one precisely agrees with the flux distribution calculated from the fixed source problem.

Table 2 Relative expansion coefficients with respect to the fundamental mode

Mode order	a_m/a_0
Fundamental	1.000
1st	−0.811
2nd	−0.114
3rd	−0.034
4th	−0.013
5th	−0.036

The Monte Carlo calculations were performed with an in-house code. Vacuum boundary conditions were imposed on both outer boundaries. The α-eigenvalues were calculated up to the first harmonic using the method developed by (Yamamoto and Miyoshi, 2003; Booth, 2003; Yamamoto, 2011b). The results of k_{eff} and α-eigenvalue calculations with the diffusion code and the in-house Monte Carlo code are listed in Table 2. The fission cross sections used in the diffusion calculations were slightly adjusted by multiplying them by 0.994963 to make the fundamental mode α-eigenvalue precisely agree with the Monte Carlo method because this study focuses on the accurate determination of the fundamental mode α-eigenvalue. The neutron count rates calculated with the diffusion code and Monte Carlo code are compared at 44 detector positions in Fig. 3 to show how closely the Monte Carlo calculation results, which are based on the transport theory, were approximated by the diffusion method. In both calculations, the neutrons were detected by capture reactions. The discontinuities of the neutron count at the material boundaries were caused by the difference of the detection efficiencies (i.e., capture cross sections).

Table 3 k_{eff} and α-eigenvalues by deterministic and Monte Carl methods

	Diffusion	Monte Carlo
k_{eff}	0.935874	0.936250 ± 0.000014
α_0 (s^{-1})	2128.7	2129.0 ± 0.2
α_1 (s^{-1})	2662.2	2700.4 ± 0.3
α_2 (s^{-1})	6928.9	—
α_3 (s^{-1})	9270.7	—

4.3 Results of Rossi-α simulation

The Monte Carlo simulation of the Rossi-α method was performed for this test problem. In this simulation, an "analog Monte Carlo" method was employed to faithfully represent a realistic stochastic random walk process. Implicit capture and Russian roulette were not used for the random walk process. The analogue Monte Carlo method was needed in order to preserve the higher moments of the distributions, although some special variance reduction techniques can be used (Yamamoto, 2011c; Szieberth et al., 2014), but it was not needed in the simple case in this paper. The number of time bin, *M*, in Eq. (14) was 5,000,000; and the time interval of each time bin, Δ, was 2×10^{-5} s. The maximum time lag index, *J*, was 200. When a particle was captured at time *t* within the mesh for the detector position, a neutron count was registered to the *m*th time bin, where

$$m = \left\lfloor \frac{t}{\Delta} \right\rfloor + 1, \tag{35}$$

and $\lfloor y \rfloor$ denotes the floor function, i.e., the largest integer not exceeding *y*. When $m > M$, the simulation was terminated, and the autocorrelations were calculated with Eq. (14). Then, the same random walk process was repeated with a different random number sequence, and new autocorrelations were obtained again. The latest estimate of the autocorrelations was added to the previous estimate. This process was repeated 100 times.

Using Eqs. (1) and (2), the autocorrelations were represented by the sum of the higher harmonic components obtained by the diffusion calculation. The diffusion-based autocorrelations as a function of the time lag are compared with the results of the Monte Carlo simulation at the three positions A, B, and C in Figs. 4, 5, and 6, respectively. The three positions are indicated in

Fig. 1. The autocorrelations are normalized at the minimum time lag $\tau = 2\times10^{-5}$ s. In these figures, the components of the fundamental mode, first, and second harmonics (i.e., $A_0(\tau, \boldsymbol{r}), A_1(\tau, \boldsymbol{r})$, and $A_2(\tau, \boldsymbol{r})$ in Eq. (2), respectively) are also shown. As seen in Figs. 4, 5, and 6, the diffusion-based autocorrelations reproduced the Monte Carlo simulation well, which verifies the higher harmonic analysis method presented in Section 2. In the fuel regions (positions A and C), the higher harmonics had a positive effect. On the other hand, they had a negative effect in the water region (position B).

The autocorrelations were fitted to a simple formula, $Ae^{-\alpha t} + B$, to obtain α. Since the higher harmonics decay faster than the fundamental mode, the α value that is closer to the fundamental mode can be obtained by excluding the earlier time lag from the fitting time span. The time span for the least squares fitting ranged from t_s to 0.004 s ($= \Delta \times 200$), where t_s is the initial time lag for the fitting. The α values obtained from the fitting are shown in Fig. 7 for several t_s. If the autocorrelations are composed of only the fundamental mode and constant term, the α values are invariant regardless of the position and t_s. However, it is not the case. While the α values in the fuel regions were larger than the fundamental mode, they were smaller in the water region. The α values approached the fundamental mode with an increase in t_s. However, the α values still significantly deviated from the fundamental mode. The higher harmonic effects cannot be completely excluded because the initial time lag, t_s, must not be too large to include the correlated component within the fitting time span.

4.4 Dual mode fitting method and better detector position

The least square fitting of dual exponential functions, $Ae^{-\alpha t} + Be^{-\alpha_1 t} + C$, (Szieberth et al., 2015) was applied to the autocorrelations. The α values obtained from the single and dual exponential functions are compared in Fig. 8. Although the higher harmonics cannot be completely discriminated from the fundamental mode with the dual exponential functions, the α values were much improved compared to the single mode fitting.

As seen in Fig. 2, the nodes of the asymmetric higher harmonic were located at the center of

the one-dimensional slab (42 cm from the outer boundaries). The effect of the first harmonic, which was the most dominant higher harmonic, vanished at the center, where an α value close to the fundamental mode α-eigenvalue is expected to be obtained by the dual mode fitting method. Fig. 8 demonstrates that the dual mode fitting method yielded almost the fundamental mode α-eigenvalue. Even with the single mode fitting method, the fundamental mode α-eigenvalue can be predicted at the center by increasing t_s as shown in Fig. 7.

5. Application of DMD to Rossi-α

5.1 DMD application to the deterministic method

Before applying the DMD method to the autocorrelations obtained from the Monte Carlo simulation where the stochastic fluctuations are included, the results of DMD applied to the diffusion-based results that are the exact numerical solutions and free from stochastic noises are presented. Using Eqs. (1) and (2), 200 snapshots of the autocorrelations were calculated at 44 detector positions. The DMD method described in Section 3 was applied to $44 \times (200-1)$ snapshot matrix $\mathbf{X}$ defined in Eq. (16). The α-eigenvalues obtained with Eq. (31) are listed up to the third harmonics in the row labeled "Case No. 1" in Table 3. The spatial distributions of the eigenvectors of the autocorrelations at the minimum time lag $\tau = 2\times10^{-5}$ s are shown in Figs. 9, 10, 11, and 12, where the DMD results (red dots) are compared with the diffusion-based numerical solutions that were obtained by summing up to the highest mode (602th mode) (solid line). For the fundamental mode (Fig. 9) and first harmonic (Fig. 10), DMD produced eigenvectors that were accurately aligned with the numerical solutions. The agreement between the two results of the eigenvectors worsened beyond the second harmonics, as seen in Figs. 10 and 11. However, the spatial distributions beyond the second harmonics were roughly reproduced by DMD. The eigenvalues of the fundamental mode and first harmonic were accurately reproduced to three digits by DMD.

In an actual neutron noise measurement, the number of detection positions must be limited owing to some experimental requirements. DMD application was tested for a total of 14 detector arrangements, as shown in Fig. 13, where the number of detection positions was reduced from 44

to 5. Note that the Rossi-α measurement does not have to be performed with many detectors being placed simultaneously. The number of detectors should be limited so as not to affect the subcriticality of the system. The Rossi-α measurement with a limited number of detectors is repeated until the autocorrelations are measured at all detector positions needed for the DMD application. In Cases 10 and 12, the detectors were allocated only in the fuel region on the left or right side, respectively. In Case 11, the detectors were allocated only in the water region between the two fuel regions. In Cases 13 and 14, the detectors were allocated only in the fuel regions. The eigenvalues obtained from DMD for the 14 detector arrangements are listed in Table 4. The fundamental mode eigenvalue, α_0, was accurately extracted even with a small number of detectors except for Case 10, where the detectors were localized in the fuel region on the left side. As seen in Fig. 4, the first harmonic of the autocorrelation was very close to the fundamental mode in the fuel region on the left side, which might render the discrimination between the two modes difficult and result in the overestimation of the fundamental mode eigenvalue for Case 10.

Table 4 Eigenvalues by DMD for deterministic results

Case No.	No. of detectors	$\alpha_0\ (s^{-1})$	$\alpha_1\ (s^{-1})$	$\alpha_2\ (s^{-1})$	$\alpha_3\ (s^{-1})$
1	44	2129.6	2665.6	6988.8	9504.2
2	15	2132.8	2697.3	7169.2	10445
3	11	2137.6	2691.0	7362.4	11553
4	9	2109.7	2666.4	6463.2	—
5	7	2156.0	2534.7	7379.7	—
6	7	2120.6	2841.1	6818.0	—
7	6	2170.9	2785.6	8192.0	—
8	5	2223.0	2732.0	9230.7	—
9	5	2172.1	3317.7	8330.0	—
10	17	2304.7	5457.2	—	—
11	12	2163.4	2879.9	8037.5	—
12	15	2228.3	3854.7	10025	—
13	32	2139.6	2735.5	7697.6	13755
14	22	2156.9	3115.8	9192.9	16871
Reference		2129.3	2662.2	6928.9	9270.7

5.2 DMD application to the stochastic method

Following the same procedure as in Sec. 5.1 for DMD application to the exact numerical results, DMD was also applied to the Monte Carlo simulation results that entail stochastic noises as in an actual measurement. The eigenvalues of the fundamental mode and first harmonic obtained from the DMD application to the Monte Carlo simulation results are listed in Table 5. The eigenvalues beyond the second harmonic were not successfully captured by DMD and are not listed in Table 4. Due to the statistical fluctuations in the autocorrelations by the Monte Carlo method, the eigenvalues extracted from DMD were not as good as those extracted by the deterministic method in Table 3 regardless of the good agreement of the autocorrelations shown in Figs. 4−6. As is well known, the DMD result is quite sensitive to measurement noise (Kutz et al., 2016; Dawson et al., 2016). Thus, the small fluctuations in the autocorrelations caused the significant differences in the eigenvalues. The eigenvalues of the higher harmonics in particular cannot be accurately determined by DMD. The fundamental mode eigenvalue, which is the most important for a subcriticality measurement, was accurately reproduced to some extent except in Cases 10 and 12, where the detectors were allocated only in the fuel region on the left or right side, respectively. The spatial distributions of the eigenvectors of the fundamental mode and the first and second harmonics are shown in Figs. 9, 10, and 11, respectively. They are compared with the diffusion-based results in the figures. The third harmonic is not shown because it was not captured by DMD, unlike the deterministic method. Although the exact solutions of the eigenvectors for the transport-based method are unknown, DMD applied to the Monte Carlo results approximately reproduced the eigenvectors of the diffusion-based results.

Table 5 Eigenvalues by DMD for Monte Carlo results

Case No.	No. of detectors	α_0 (s^{-1})	α_1 (s^{-1})
1	44	2202.5	3728.3
2	15	2180.2	4413.5
3	11	2181.8	4926.1
4	9	2146.3	5170.9
5	7	2120.7	6989.2
6	7	2067.6	6161.7
7	6	2115.0	5132.3
8	5	2057.9	5963.8
9	5	2171.2	6121.2
10	17	2443.1	7437.4
11	12	2020.8	4524.0
12	15	2661.4	13761
13	32	2213.7	5954.1
14	22	2262.9	7321.0
Reference		2129.0 ± 0.2	2700.4 ± 0.3

6. Conclusions

An exact formula for the joint probability of a pair neutron detection between two different detection times was revisited in this study. Within the limit of the diffusion approximation, the autocorrelations in a one-dimensional, two-energy group subcritical system was represented by the sum of a large number of higher harmonics. Since the autocorrelations as a function of the time lag reproduced the results of the Monte Carlo simulations for the Rossi-α method well, the formula and numerical method used in this study are considered to be valid.

DMD was applied to the Rossi-α method to extract the fundamental mode and major higher harmonics of the α-eigenvalue mode from the autocorrelations. The autocorrelations obtained from the deterministic diffusion method, which were free from stochastic noise, were accurately decomposed into higher harmonic components up to the third order. The accuracy worsened with the decrease in the number of detection positions. The detection positions should cover the wider range of the subcritical system so that DMD can yield more accurate eigenvalues even if a limited

number of detection positions are available. On the other hand, localizing the detection positions in a given region should be avoided to prevent enhancing the undesirable effect of a localized higher harmonic.

In addition to using the results of the deterministic diffusion method, DMD was also applied to the autocorrelations obtained from the Monte Carlo simulation that included stochastic noise, such as an actual noise measurement. DMD did not work as well as the deterministic results due to the stochastic noise in the Monte Carlo simulation. However, if detection positions are properly allocated within a subcritical system, DMD could yield a satisfactorily accurate fundamental mode α-eigenvalue from the autocorrelations that include the stochastic noises. Since this study may be the first attempt to apply DMD to the neutron noise technique for subcriticality measurements, a comprehensive trial for a three-dimensional, continuous energy subcritical system should be included in future work.

References

Abdo, M., Elzohery, R., Roberts, J.A., 2019. Modeling isotopic evolution with surrogates based on dynamic mode decomposition. Ann. Nucl. Energy 129, 280–288. https://doi.org/10.1016/j.anucene.2019.01.048.

Berglöf, C., Fernández-Ordóñez, M., Villamarín, D., Bécares, V., González-Romero, E.M., Bournos, V., Muñoz-Cobo, J.L., 2011. Auto-correlation and variance-to-mean measurements in a subcritical core obeying multiple alpha-modes. Ann. Nucl. Energy, 38, 194–202. https://dx.doi.org/10.1016/j.anucene.2010.11.009.

Booth, T.E., 2003. Computing the higher *k*-eigenfunctions by Monte Carlo power iteration: a conjecture. Nucl. Sci. Eng. 143, 291–300. https://dx.doi.org/10.13182/NSE02-10TN.

Dawson, S.T.M., Hemati M.S., Williams, M.O., Rowley, C.W., 2016. Characterizing and correcting for the effect of sensor noise in the dynamic mode decomposition. Exp. Fluids 57:42. https://link.springer.com/article/10.1007/s00348-016-2127-7.

Di Ronco, A., Introini, C., Cervi, E., Lorenzi, S., Jeong, Y.S., Seo, S.B., Bang, I.C., Giacobbo, F.,

Cammi, A., 2020. Dynamic mode decomposition for the stability analysis of the Molten Salt Fast Reactor core. Nucl. Eng. Des. 362, 110529. https://doi.org/10.1016/j.nucengdes.2020.110529.

Endo, T., Yamane, Y., Yamamoto, A., 2006. Space and energy dependent theoretical formula for the third order neutron correlation technique. Ann. Nucl. Energy 33, 521–537. https://dx.doi.org/10.1016/j.anucene.2006.02.002.

Feynman, R.P., De Hoffman, F., Serber, R., 1956. Dispersion of the neutron emission in U-235 fission. J. Nucl. Energy 3, 64–69.

Hardy, Z.K., Morel, J.E., Ahrens, C., 2019. Dynamic mode decomposition for subcritical metal systems. Nucl. Sci. Eng. 193 1173–1185. https://doi.org/10.1080/00295639.2019.1609317.

Iijima, T. Sugi, T., Ezure, H., Kasai, M., 1968. Space-dependent effects in Rossi-alpha experiments. Nucl. Sci. Eng. 33, 344–348. https://doi.org/10.13182/NSE68-A19245.

Katano, R., 2019. Estimation method of prompt neutron decay constant reducing higher order mode effect by linear combination. Nucl. Sci. Eng. 193, 431–439. https://doi.org/10.1080/00295639.2018.1528803.

Kitamura, Y., Matoba, M., Misawa, T., Unesaki, H., Shiroya, S., 1999. Reactor noise experiments by using acquisition system for time series data of pulse train. J. Nucl. Sci. Technol. 36, 653–660. https://doi.org/10.1080/18811248.1999.9726252.

Kópházi, J., Lathouwers, D., 2012. Three-dimensional transport calculation of multiple alpha modes in subcritical systems. Ann. Nucl. Energy 50, 167–174. https://doi.org/10.1016/j.anucene.2012.06.021.

Kutz, J.N., Brunton, S.L., Proctor, J.L., 2016. Dynamic mode decomposition: Data-driven modeling for complex systems, Society for Industrial and Applied Mathematics, Philadelphia, Pennsylvania. https://doi.org/10.1137/1.9781611974508.

McClarren, R.G., 2019. Calculating time eigenvalues of the neutron transport equation with dynamic mode decomposition. Nucl. Sci. Eng. 193, 854–867. https://doi.org/10.1080/00295639.2018.1565014.

McClarren, R.G., Haut, T.S., 2020. Data-driven acceleration of thermal radiation transfer calculations with the dynamic mode decomposition and a sequential singular value decomposition. arXiv preprint arXiv:2009.11686.

Muñoz-Cobo, J.L., Berglöf, C., Peña, J., Villamarín, D., Bournos, V., 2011. Feynman-α and Rossi-α formulas with spatial and modal effects. Ann. Nucl. Energy 38, 590–600. https://doi.org/10.1016/j.anucene.2010.09.027.

Orndoff, J.D., 1957. Prompt neutron periods of metal critical assemblies. Nucl. Sci. Eng. 2, 450–460. https://dx.doi.org/10.13182/NSE57-A25409.

Roberts, J.A., Xu, L., Elzohery, R., Abdo, M., 2019. Acceleration of the power method with dynamic mode decomposition. Nucl. Sci. Eng. 193, 1371–1378. https://doi.org/10.1080/00295639.2019.1634928.

Schmid, P.J., 2010. Dynamic mode decomposition of numerical and experimental data. J. Fluid Mech. 656, 5–28. https://doi.org/10.1017/S0022112010001217.

Szieberth, M., Kloosterman, J.L., 2014. Unbiased estimators of coincidence and correlation in non-analogous Monte Carlo particle transport. Ann. Nucl. Energy 73, 270–281. https://doi.org/10.1016/j.anucene.2014.06.034.

Szieberth, M., Klujber, G., Kloosterman, J.L, de Haas, D., 2015. Measurement of multiple α-modes at the Delphi subcritical assembly by neutron noise techniques. Ann. Nucl. Energy 75, 146–157. https://dx.doi.org/10.1016/j.anucene.2014.07.018.

Szieberth, M., German, P., Nagy, L., Kópházi, J., Lathouwers, D., 2017. Calculation of the higher alpha modes of the VENUS-F fast subcritical system. In Proc. of M&C 2017 – Int. Conf. Mathematics & Computational Methods Applied to Nuclear Science & Engineering, Jeju, Korea, April 16-20, 2017. Korean Nuclear Society. https://www.kns.org/files/int paper/paper/MC2017 2017 4/P205S04-03SzieberthM.pdf.

Talamo, A., Gohar, Y., Sadovich, S., Kiyavitskaya, H., Bournos, V., Fokov, Y. Routkovskaya, C., 2013. Correction factor for the experimental prompt neutron decay constant. Ann. Nucl. Energy 62, 421–428. https://dx.doi.org/10.1016/j.anucene.2013.06.035.

Talamo, A., Gohar, Y. Yamanaka, M., Pyeon, C.H., 2020. Calculation of the prompt neutron decay constant for the KUCA facility driven by a stationary or pulsed external neutron source. J. Nucl. Sci. Technol. 57, 145–156. https://doi.org/10.1080/00223131.2019.1651232.

Uyttenhove, W., Lathouwers, D., Kloosterman, J., van der Hagen, T.H.J.J., Van den Eynde, G., Baeten, P., 2014. Methodology for modal analysis at pulsed neutron source experiments in accelerator driven systems. Ann. Nucl. Energy 72, 286–297. https://doi.org/10.1016/j.anucene.2014.05.007

Yamamoto, T., Miyoshi, Y., Tonoike, K., Okamoto, H., Ida, T., Aoki, S, 2003. Effect of higher-harmonics flux in exponential experiment for subcriticality measurement. J. Nucl. Sci. Tehcnol. 40, 77–83. https://doi.org/10.1080/18811248.2003.9715336.

Yamamoto, T., Miyoshi, Y., 2003. An algorithm of α- and γ-mode eigenvalue calculations by Monte Carlo method. Proc. 7th Int. Conf. on Nuclear Criticality Safety (ICNC'03), JAERI-Conf 2003-019, Japan Atomic Energy Research Institute, Tokai, Japan, October 2003.

Yamamoto, T., 2011a. Higher order mode analyses in Feynman α method. Ann. Nucl. Energy 38, 1231–1237. https://dx.doi.org/10.1016/j.anucene.2011.02.017.

Yamamoto, T., 2011b. Higher order α mode eigenvalue calculation by Monte Carlo power iteration. Prog. Nucl. Sci. Technol. 2, 826–835. https://dx.doi.org/10.15669/pnst.2.826.

Yamamoto, T., 2011c. Applicability of non-analog Monte Carlo technique to reactor noise simulation. Ann. Nucl. Energy 38, 647–655. https://doi:10.1016/j.anucene.2010.09.004.

Yamamoto, T., 2014. Higher order mode analyses of power spectral density and Feynman-α method in accelerator driven system with periodically pulsed spallation neutron source. Ann. Nucl. Energy 66, 63–73. https://dx.doi.org/10.1016/j.anucene.2013.12.002.

Yamamoto, T., 2015. Higher harmonic analyses of the ^{252}Cf source driven noise analysis method. Ann. Nucl. Energy 76, 521–529. https://dx.doi.org/10.1016/j.anucene.2014.10.034.

Yamamoto, T., Sakamoto, H., 2019. Decomposition of neutron noise in a reactor into higher-order mode components and investigation of the space and frequency dependence. Prog. Nucl. Energy 117, 103098. https://doi.org/10.1016/j.pnucene.2019.103098.

Yamamoto, T., Sakamoto, H., 2021. Application of dynamic mode decomposition to exponential experiment for spatial decay constant determination. Ann. Nucl. Energy 162, 108506. https://dx.doi.org/10.1016/j.anucene.2021.108506.

List of figures

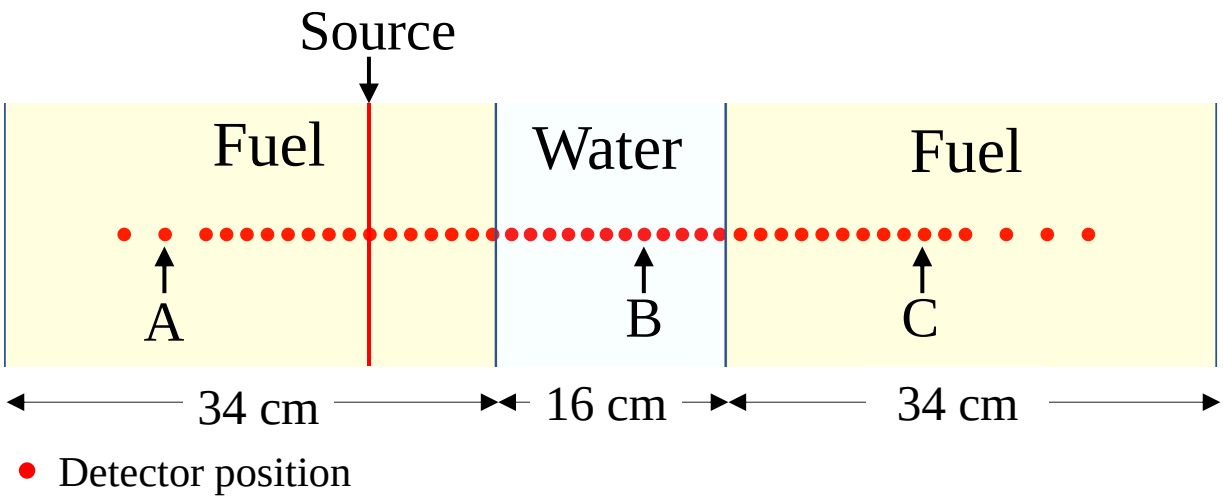

Fig. 1 One-dimensional geometry for the test problem, detector and source positions

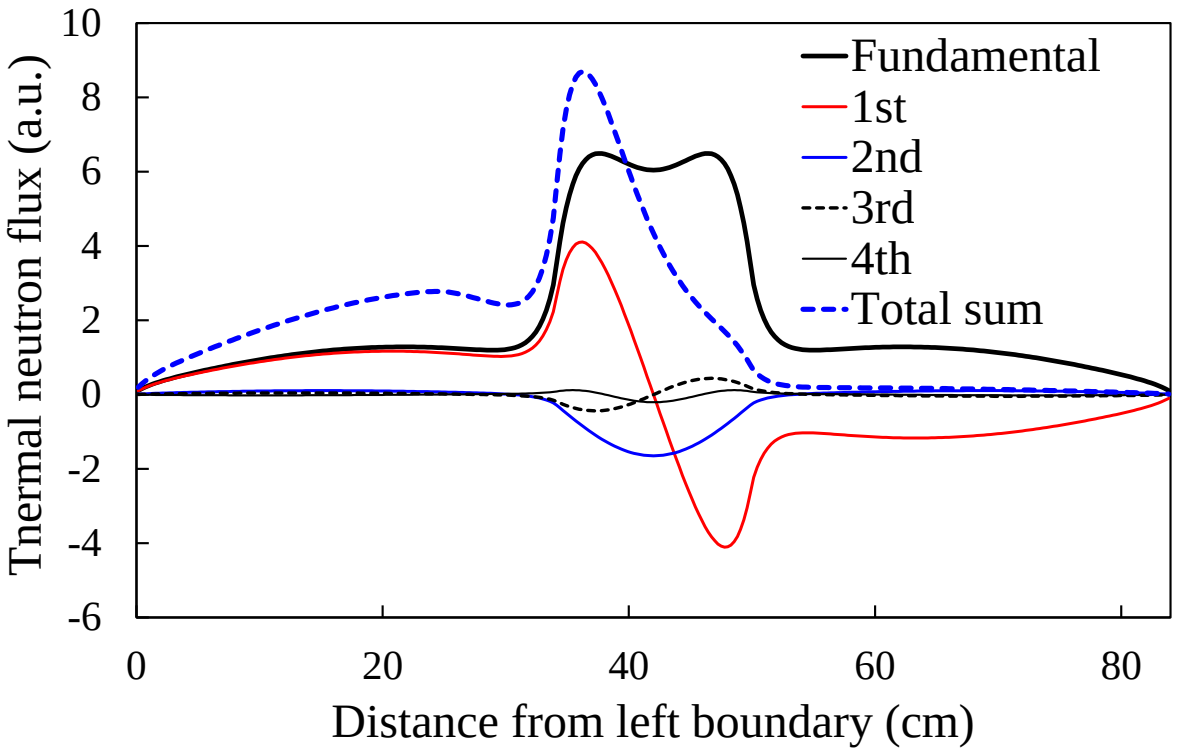

Fig.2 Decomposed higher harmonics of steady-state thermal neutron flux distribution

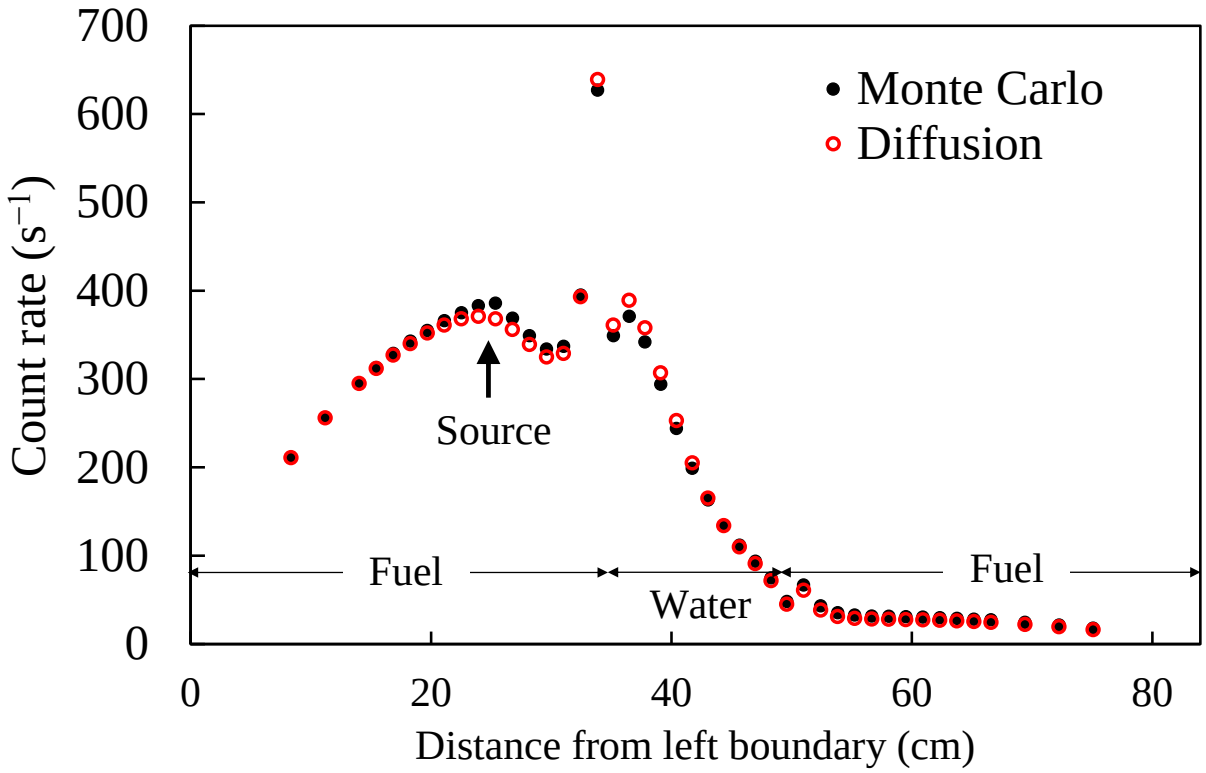

Fig. 3 Neutron count rate distribution by the diffusion method and Monte Carlo method

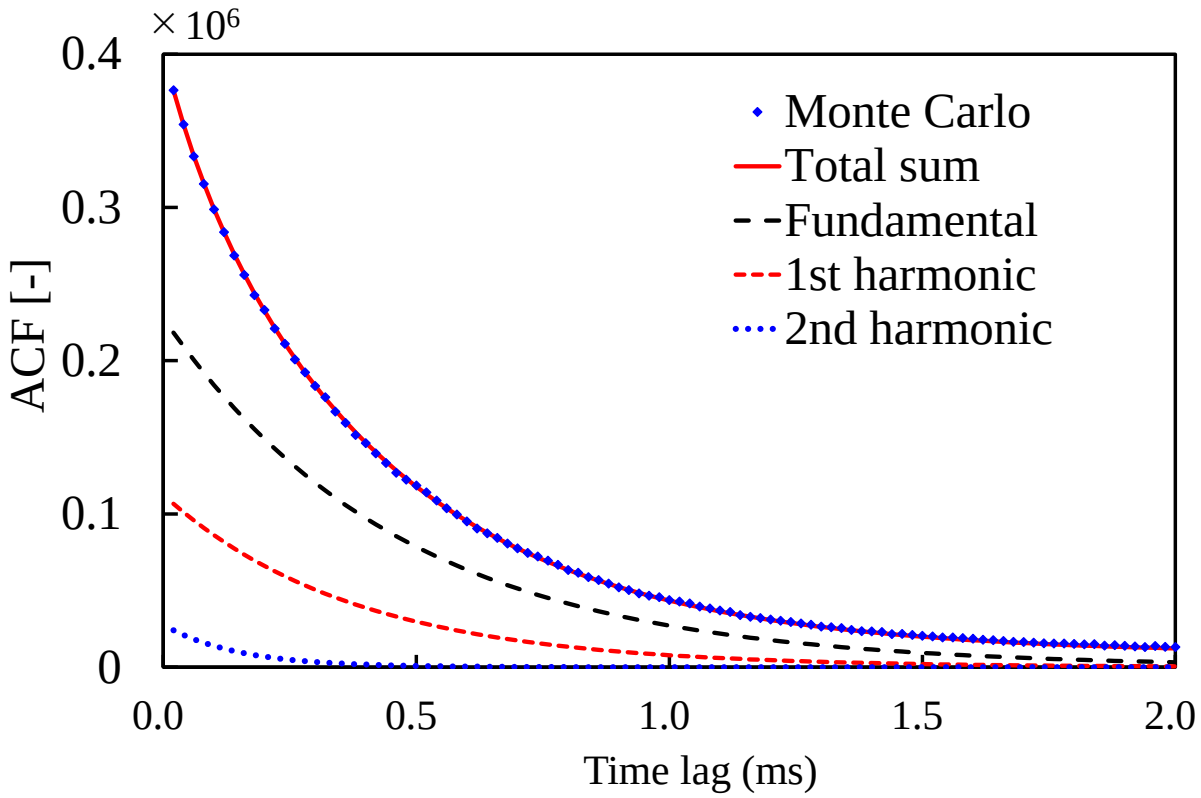

Fig. 4 Autocorrelation functions by Monte Carlo simulation and diffusion method at position A

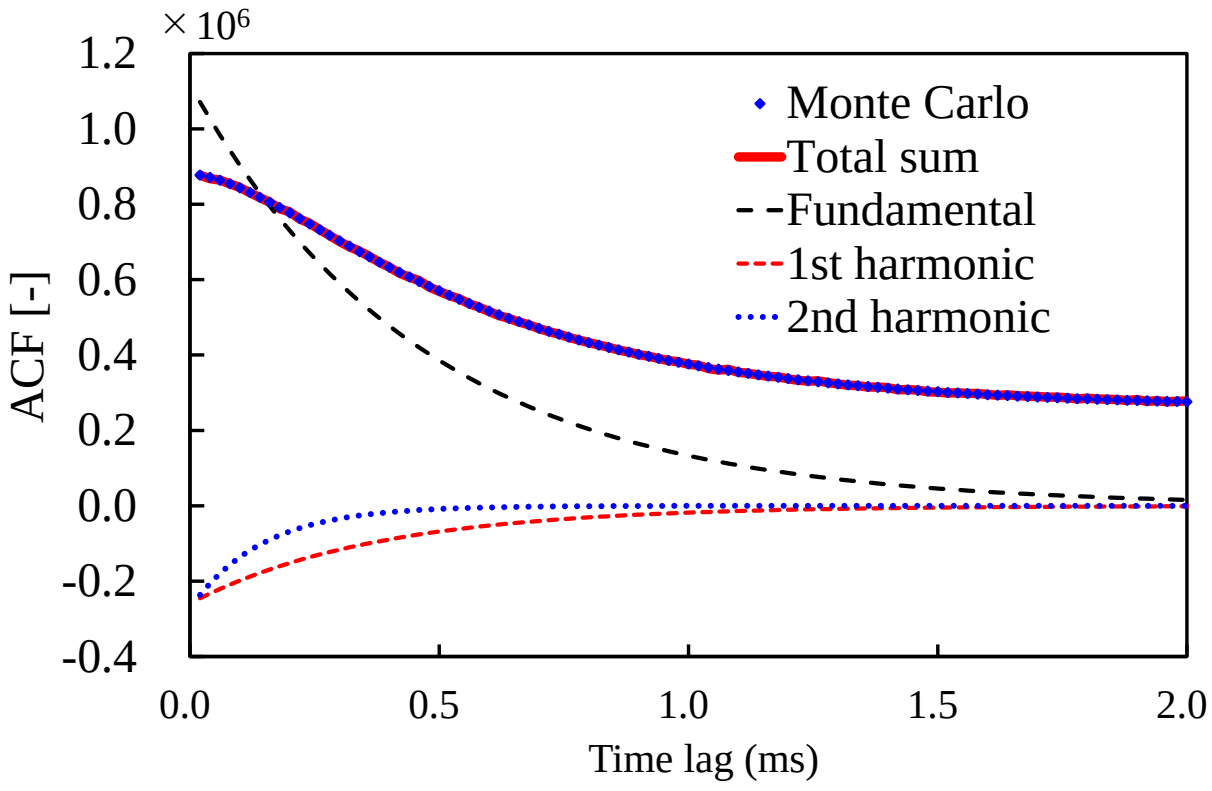

Fig. 5 Autocorrelation functions by Monte Carlo simulation and diffusion method at position B

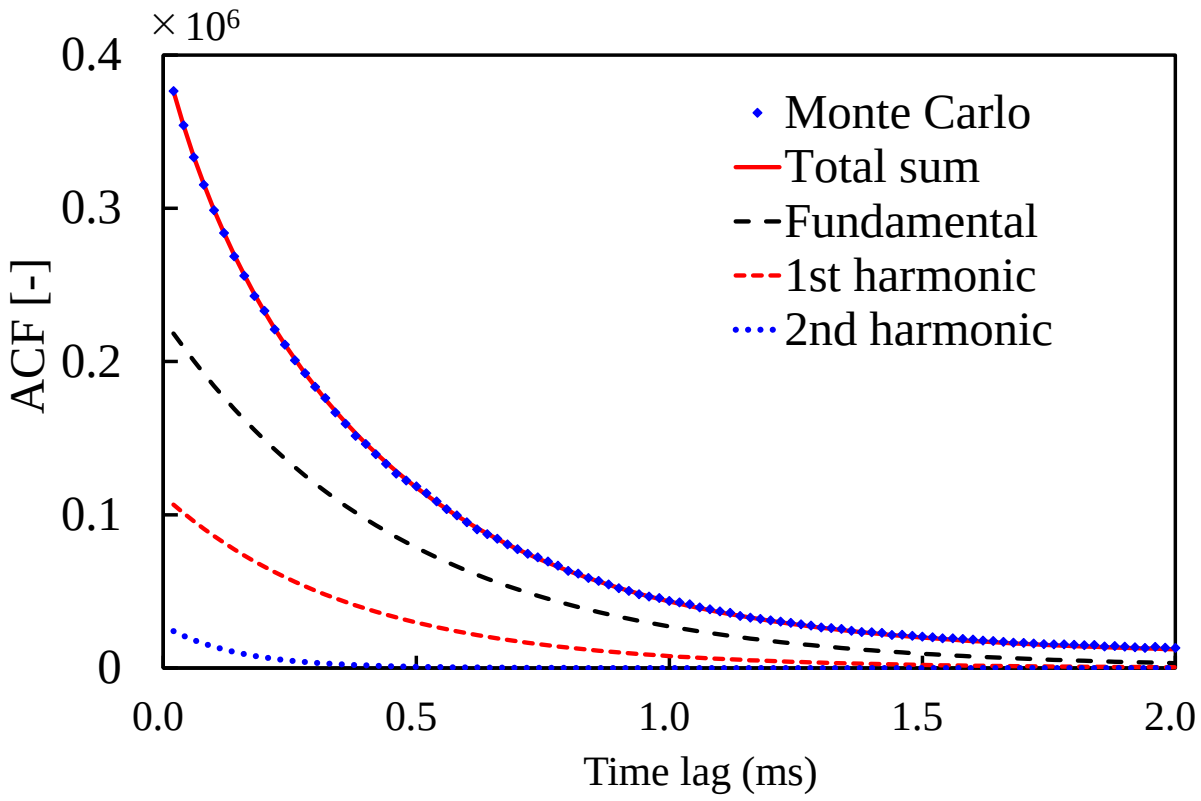

Fig. 6 Autocorrelation functions by Monte Carlo simulation and diffusion method at position C

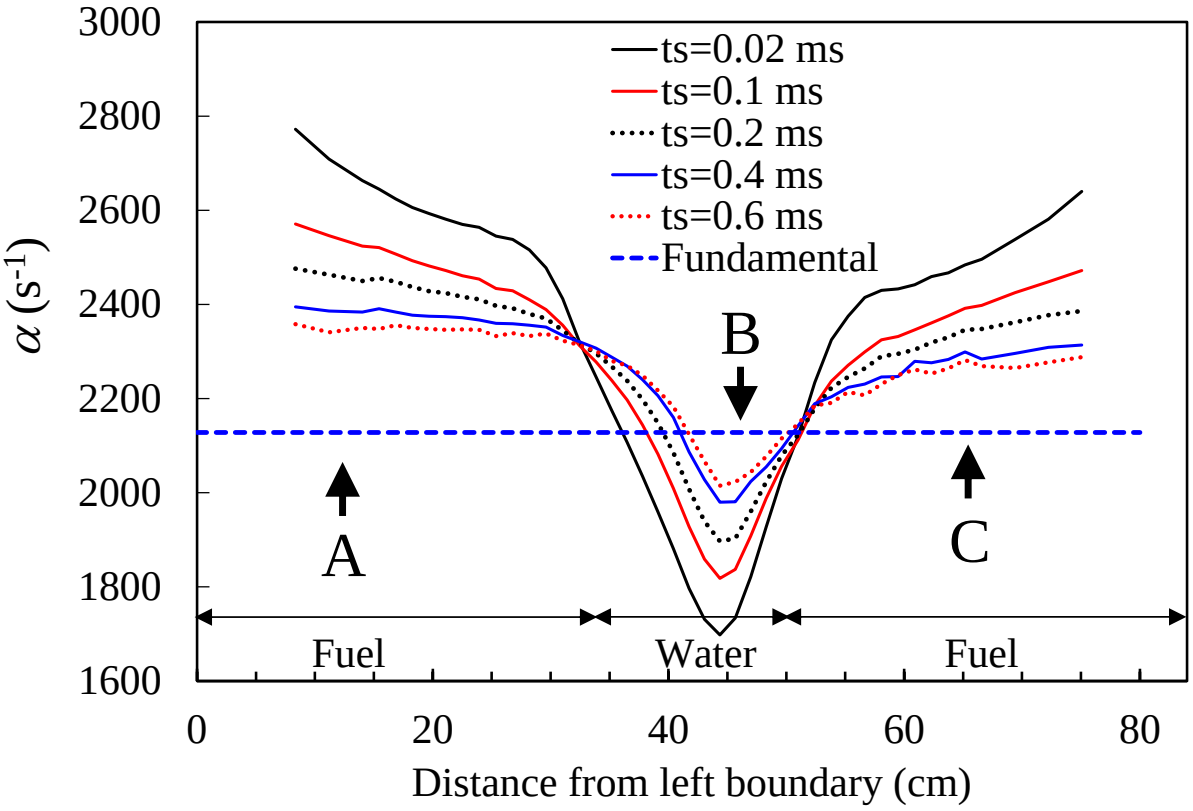

Fig. 7 α values by least squares fitting to $Ae^{-\alpha t} + B$. The time span for fitting starts with t_s.

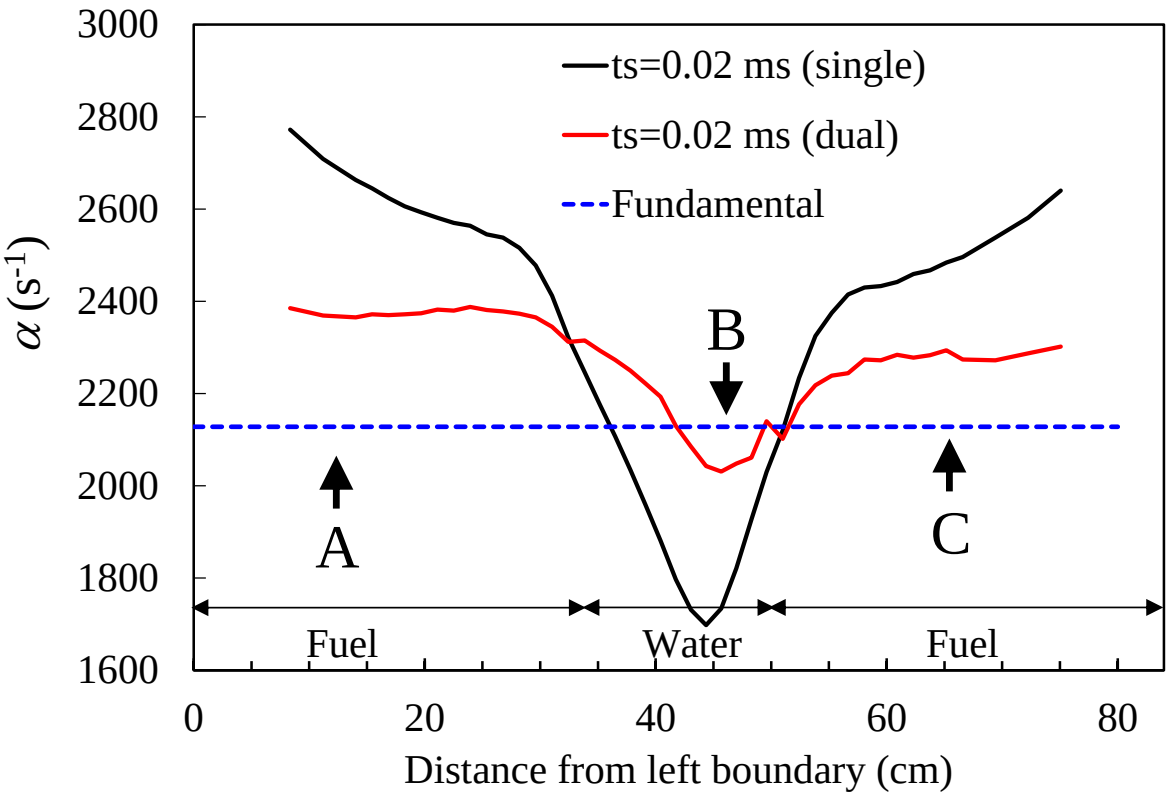

Fig. 8 Comparison of α values between the single and dual exponential fittings

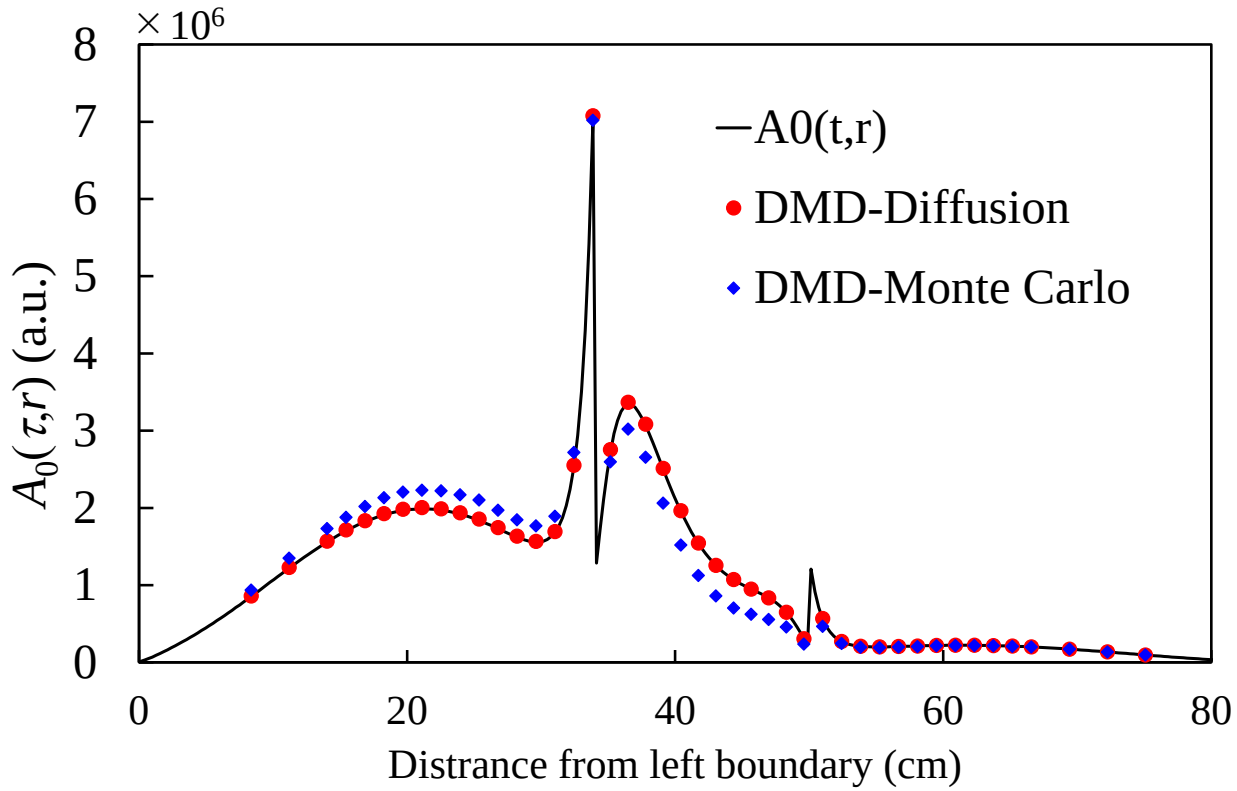

Fig. 9 Fundamental mode of the autocorrelation function by Eq. (2) and DMD (diffusion and Monte Carlo)

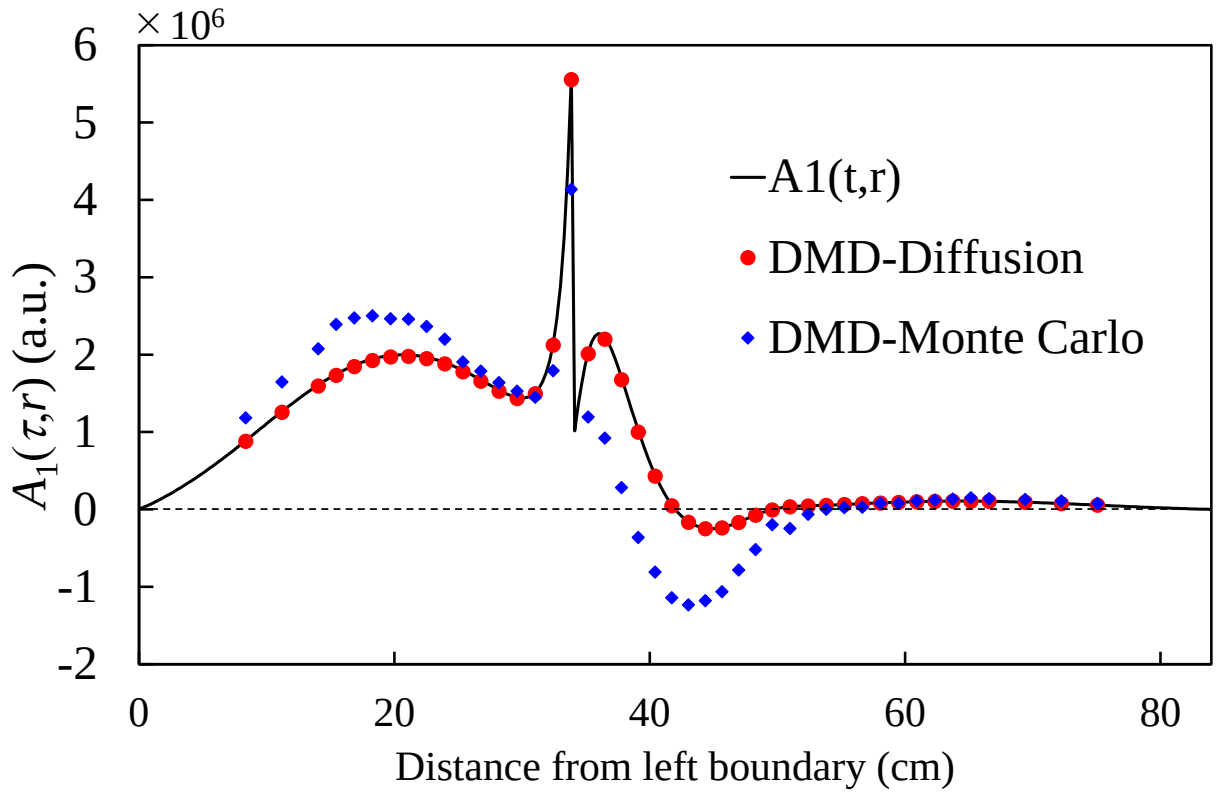

Fig. 10 First harmonic of autocorrelation function by Eq. (2) and DMD (diffusion and Monte Carlo)

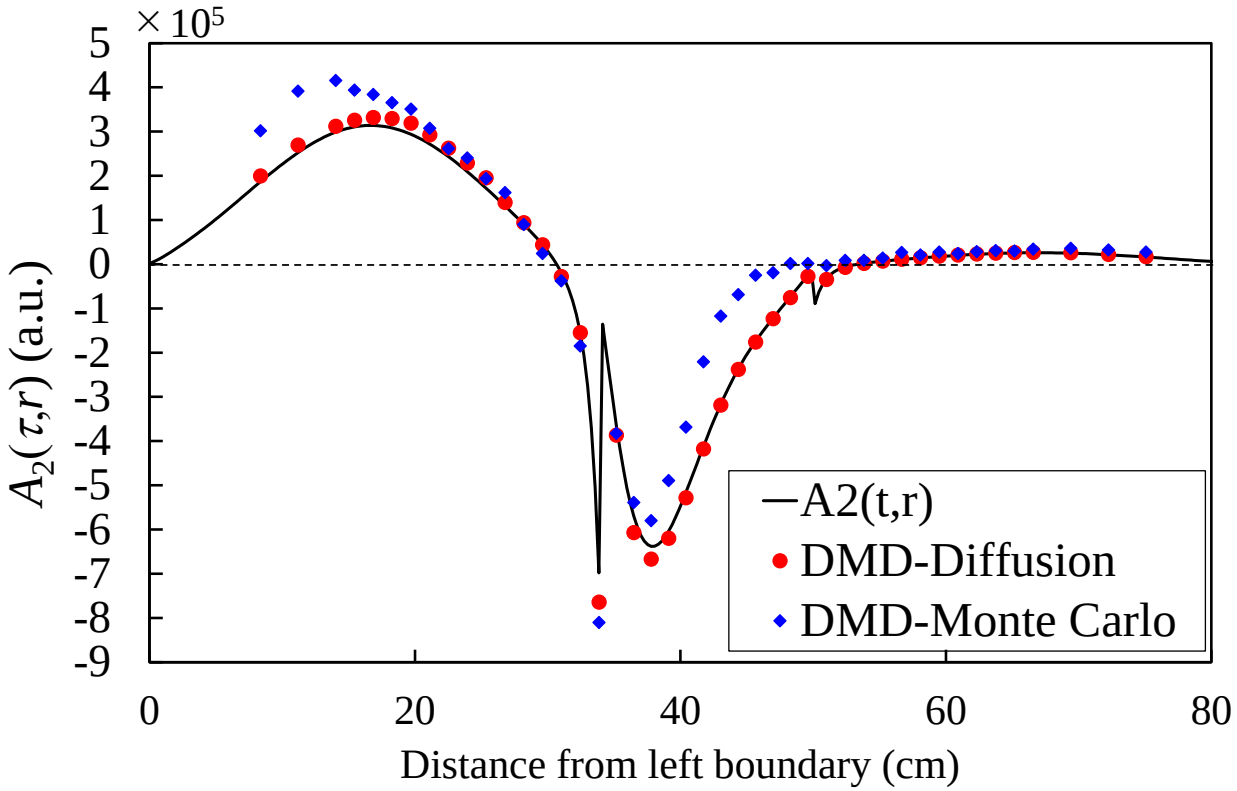

Fig. 11 Second harmonic of autocorrelation function by Eq. (2) and DMD (diffusion and Monte Carlo)

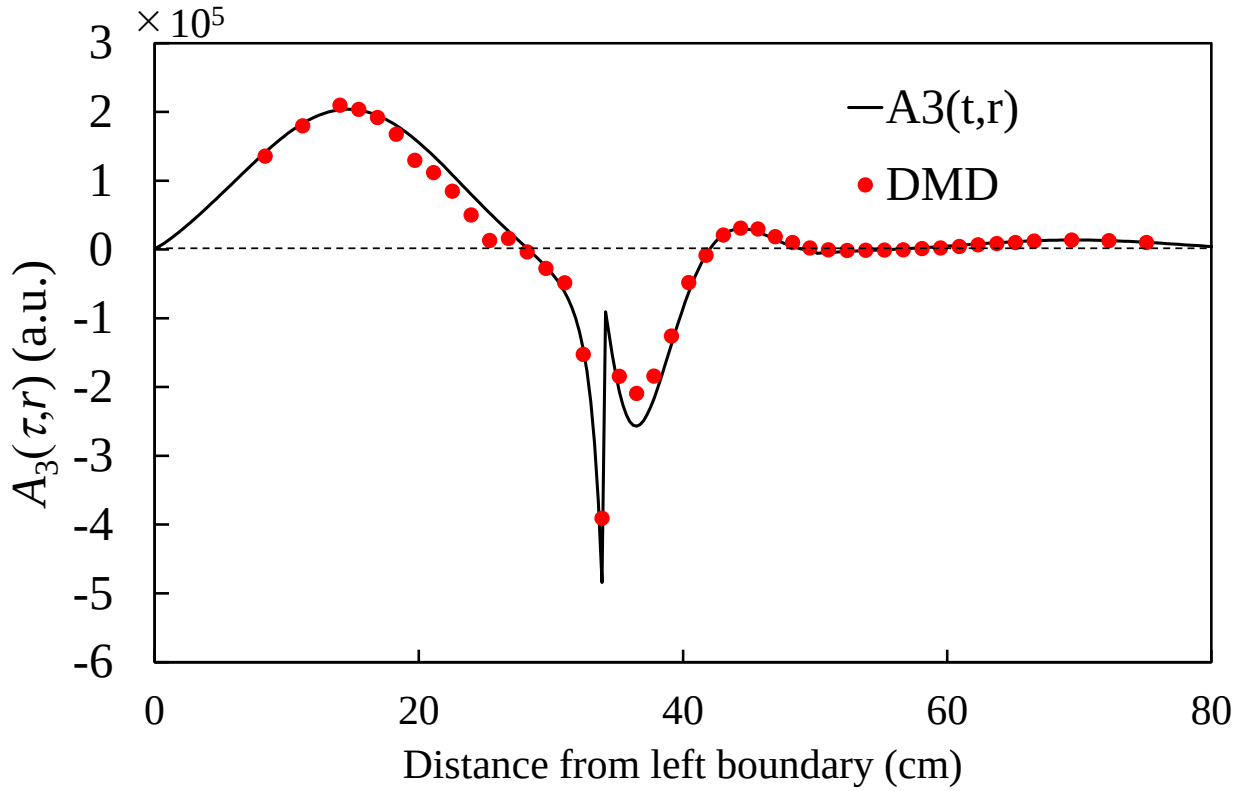

Fig. 12 Third harmonic of the autocorrelation function by Eq. (2) and DMD (diffusion)

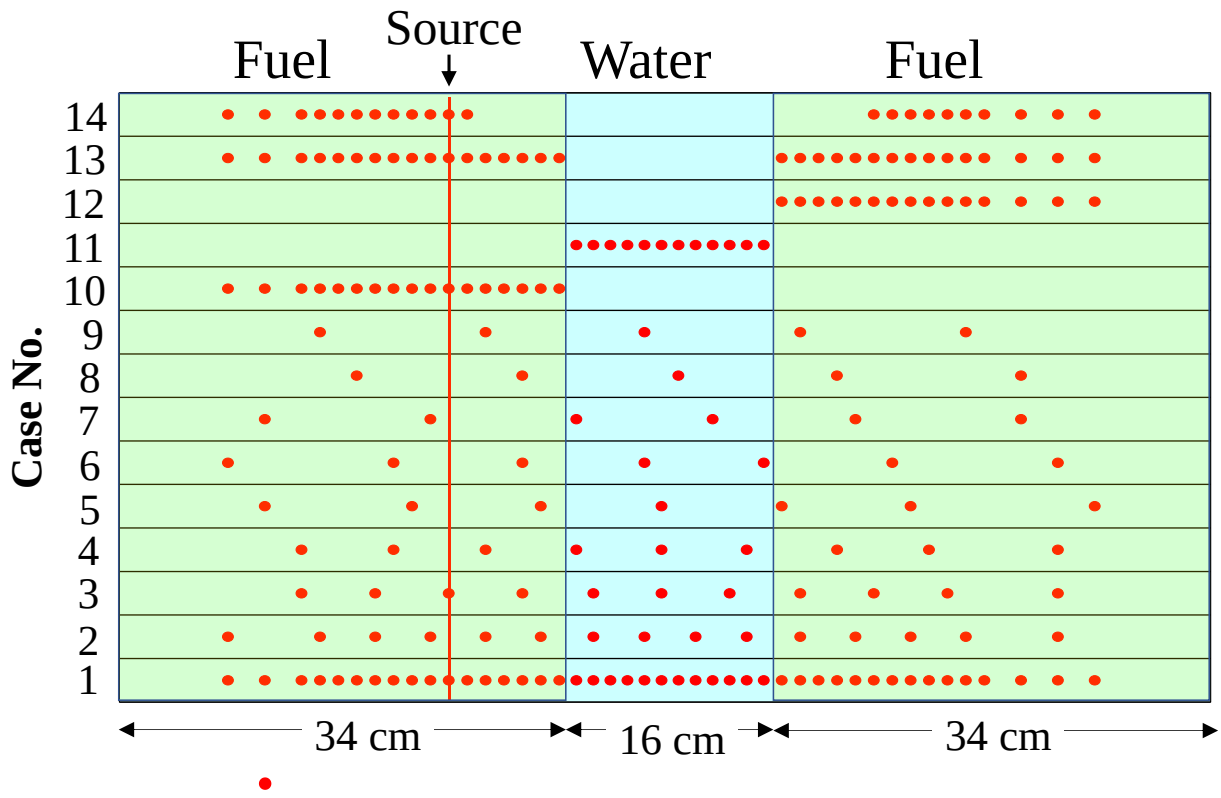

Fig. 13 Arrangements of detector positions for DMD (numerical data of detector positions are presented in an excel file as “Supplementary material”)

CRediT authorship contribution statement

Toshihiro Yamamoto: Supervision, Methodology, Conceptualization, Investigation, Writing - original draft. **Hiroki Sakamoto**: Software, Validation, Formal analysis, Data curation, Writing - review & editing.

Declaration of interest statement

The authors declare no conflicts of interest associated with this manuscript.